Available online at www.sciencedirect.com

jmr&t
Journal of Materials Research and Technology
www.jmrt.com.br

Original Article

Macro and microgalvanic interactions in friction stir weldment of AA2198-T851 alloy

Uyime Donatus, Rejane Maria Pereira da Silva, João Victor de Sousa Araujo, Mariana Xavier Milagre, Caio Palumbo de Abreu, Caruline de Souza Carvalho Machado, Isolda Costa*

Nuclear and Energy Research Institute, Av. Prof. Lineu Prestes, 2242 São Paulo, Brazil

ARTICLE INFO

Article history:
Received 8 March 2019
Accepted 8 October 2019
Available online 6 November 2019

Keywords:
Aluminium
Polarization
SEM
Pitting corrosion
Oxygen reduction
Friction stir welding

ABSTRACT

The galvanic interactions within and between the friction stir weld zones of the AA2198-T851 alloy have been investigated using electrochemical and microscopy techniques. The parent material (PM) was the most anodic region and exhibited pronounced severe localized corrosion (SLC) both when coupled and isolated. The stir zone was the most resistant to corrosion and exhibited no SLC when coupled, but exhibited SLC when isolated. Profiles associated with dissolved oxygen consumption and hydrogen generation currents across the weldment were inversely related because the anodic (PM) region produced higher hydrogen bubbles and, interestingly, consumed more dissolved oxygen compared with the other regions.

1. Introduction

New generation Al-Cu-Li alloys are currently being employed for aerospace application because of their relative specific strength when compared with conventionally used 2xxx and 7xxx aerospace alloys [1]. An addition of 1% Li into the alloy results in a 3% decrease in density and a 6% increase in the elastic modulus [1,2]. The new generation alloys have been designed to overcome the corrosion and mechanical challenges posed by the 1st and 2nd generation Al-Li alloys [1,2]. This is achieved by optimising the alloying additions and the thermomechanical processing routes [1].

However, these alloys are still very much susceptible to localized corrosion, with even more corrosion challenges after welding [3–6]. This is because welding significantly modifies the microstructure of the alloy and results in macro-galvanic coupling in addition to the inherent micro-galvanic couples in the parent material.

Currently, the most proposed welding process for Al alloys is friction stir welding and for apparent reasons. It is a solid-state welding process that is capable of producing joints with less distortion, reduced heat-affected zone and without the problems associated with fusion welding processes such as liquation and solidification cracking, porosity, and slag inclusion. Additionally, the friction stir

* *Corresponding author.*
E-mail: uyimedonatus@yahoo.com (U. Donatus).
https://doi.org/10.1016/j.jmrt.2019.10.015

welding process is autogenous and does not produce toxic fumes.

Nonetheless, a friction stir weldment has four distinct zones: the dynamically recrystallised stir zone (SZ), the mechanically deformed thermomechanically affected zone (TMAZ), the heat-affected zone (HAZ) and the unaffected parent metal (PM). These zones have their individual characteristic microstructural and metallurgical features that result in varying electrochemical responses across the weldment.

For the new generation Al-Cu-Li alloys in the peak-age temper (T8) condition, the friction stir welding process results in the coarsening and dissolution of the major strengthening hexagonal T1 (Al_2CuLi) phase as the weld centre is approached [6]. Thus, the PM contains the highest volume of the T1 phase followed by the HAZ and TMAZ with the SZ having the least [6]. The T1 phase is highly active and results in the dissolution of the matrix when the alloy is exposed to an aggressive environment [7–9]. To further stress the importance of microstructure on the corrosion behaviour of the new generation Al-Cu-Li alloys, Huang et al. [10] recently carried out an experiment to show that temper conditions significantly dictate the corrosion type and morphology in Al-Cu-Li alloys. For a temper condition that promotes the precipitation of T1 phase inside the grains, an intragranular form of corrosion would be observed. On the other hand, a temper that promotes subgrain boundary and grain boundary precipitation of T1 particles would result in the formation of subgrain-boundary attacks and intergranular corrosion. However, in contrast to most reports, Yan et al. [11] recently reported that the development of localized corrosion in different tempers of the AA2050 alloy could not be associated with the T1 phase because its thickness range is so small and far below the critical size for the inducement of localized corrosion [12–14]. However, it was clearly revealed in the work of Zhang et al. [5] and one of our works [15] that the non-uniform precipitation of the T1 phase along $\{111\}_{Al}$ inside the grains of Al-Cu-Li alloys with T6 [5] and T851 [15,16] tempers was responsible for the corroded bands often observed in these alloys. Nonetheless, it is clear that mechanical deformation and thermal treatments influence the precipitation sequence and the regions of precipitation of the active phases in Al-Cu-Li alloys.

The friction stir welding process induces different degrees of mechanical deformation and thermal gradients, such that, in a weldment of a precipitation-hardened Al-Cu-Li alloy, the different regions created by the process experience different types of precipitation with the exhibition of different corrosion characteristics. In recently published works by the same authors, it was shown that the PM is the most susceptible region (due to the prevalence of T1 particles) while the SZ is the most resistant region (due to the absence of T1 particles) in a friction stir weldment of an AA2198-T851 alloy which is a representative member of the new generation alloy [4,6]. But works by other authors show different regions that are most susceptible to corrosion in weldments of different new generation alloys [3,17–19]. However, the primary purpose of the current study is to give details about the micro and macro-galvanic interactions within and between the zones of the friction stir weldment of the AA2198-T851 alloy which has not been elucidated elsewhere. Thus, the present study presents macro-galvanic interactions within the SZ, and between the SZ/TMAZ/HAZ and the PM using potentiodynamic polarization, immersion test, scanning electrochemical microscopy (SECM), and scanning electron microscopy (SEM). Information regarding the extents of oxygen consumption and hydrogen evolution across the weldment as revealed using SECM is also presented in this study. Use of SECM in the study of the galvanic interactions across the weldment of Al alloys is scarce in the literature. Thus, the SECM results in this study contribute significantly to the body of knowledge on corrosion behaviours of friction stir weldments of Al alloys.

2. Materials and method

A friction stir weldment of AA2198-T851 (Al-3.31Cu-0.96Li-0.31Mg-0.04Fe-0.03Si-0.25Ag-0.4Zr (wt. %)) alloy was employed for this investigation. The welding was carried out using a traverse speed of 150 mm/min and a rotation rate of 800 rpm. The diameter of the tool shoulder was 6 mm while that of the pin was 2 mm and the penetration depth was 1.9 mm.

All the samples were sequentially polished to a 1 μm surface finish using SiC papers and diamond pastes before any test.

The corrosion tests were conducted in a naturally aerated 5 mM NaCl solution at room temperature. Corrosion immersion test was performed for 72 h. Three samples were exposed: a sample from the PM region; a sample from the SZ/TMAZ region; and a sample comprising the PM, SZ, TMAZ and HAZ in the advancing side (AS) of the weldment. This was carried out to establish the effect of galvanic coupling.

Potentiodynamic polarization tests were carried in a 5 mM NaCl solution in an aerated environment at room temperature (25 °C) and were conducted for the PM and SZ/TMAZ samples using a Bio-Logic potentiostat. A Ag/AgCl saturated KCl reference electrode and a platinum wire electrode were employed in a three-electrode cell set-up. The polarization scan was from −200 mV of the open circuit potential (OCP) to +800 mV of the OCP, after a 1.5 h OCP measurement and the scan rate was 1 mV/s. The samples were coated with beeswax to expose a surface area of 0.25 cm^2 prior to the measurements. The tests were repeated four times to ensure reproducibility, and freshly prepared samples and solutions were used in each case.

Scanning electrochemical microscopy (SECM) was carried out on a sample comprising the PM, HAZ, TMAZ and SZ, in the advancing side of the weldment. The results were obtained in the AS of the weldment from the centre of the SZ to the HAZ/PM side of the weldment (9 mm from the weld centreline). The experiments were conducted using a microscope built by SensolyticsGmbH in Bochum Germany. The tests were performed at room temperature with the sample in open circuit potential (OCP). An electrochemical cell was utilized with a 25 μm (12.5 μm radius (a))Pt disk ultra-micro-electrode (tip) as a working electrode, Ag/AgCl(saturated KCl) as a reference electrode and platinum as the counter electrode.

For the calibration of the tip, prior to the SECM measurements, cyclic voltammetry (CV) of 5 mM $L^{-1}K_4[Fe(CN)_6]$ in 100 mM L^{-1}KCl was performed to ensure that the system was well-calibrated, and a sigmoidal shaped CV was obtained. The CV data also provides the steady-state diffusion-controlled limiting current (i_{lim},). The tip potential was set at +0.40 V

Ag/AgCl, to perform the oxidation of ferrocyanide to ferricyanide ions at the tip:

$$Fe(CN)_6^{4-} \leftrightarrow Fe(CN)_6^{3-} + e^- \quad (1)$$

The limiting current (i_{lim}) is a function of microelectrode radius (a), the concentration of the species (c) and its diffusion coefficient (D), as shown by the following equation [20]:

$$i_{lim} = 4nFDCa \quad (2)$$

For the measurements of currents associated with oxygen consumption and hydrogen evolution, experiments were made at selected heights above the sample. The operating height was set after recording z-approach curves, with the tip adjusted to 20 μm (constant height (d)) above the surface. After setting the height, measurements were then obtained by scanning the tip in the x (lines) and x–y plane (maps) and recording the tip current as a function of its location.

Differential Scanning Calorimetry (DSC) tests were conducted using a DSC-50 SHIMADZU equipment coupled to TA-60WS. The tests were conducted in nitrogen (99.999 wt%) atmosphere. Before the tests, the samples were ground with silicon carbide paper, and samples weighing in the range of 20–30 mg were cut for the tests. A heating rate of 10 °C/min from scanning temperature 50 °C to 550 °C was employed for the collection of the DSC data.

The microstructural examination was conducted using a Leica DMLM coupled optical microscope and a JEOL JSM-6010LA scanning electron microscope. Transmission electron microscopy was carried out using a JEOL 2100 microscope. Bright-field and high angle annular dark-field (HAADF) images were obtained, and the samples were prepared by twin-jet electropolishing using a solution comprising 20% HNO_3 in methanol at −30 °C.

3. Results and discussion

This section presents the extent of galvanic contributions to the corrosion susceptibilities in the individual zones of the weldment. This is achieved by quantifying the current distribution attributed to oxygen reduction and hydrogen evolution in a galvanic couple of the weldment (i.e., by exposing all the zones of the weldment in the combined form). And also by showing the effect of selectively exposing the bulk cathodic and anodic regions separately.

3.1. *Optical and SEM examination of corrosion evolution*

Presented in Fig. 1 is an optical image of the weldment after a 72 h immersion test in 5 mM NaCl solution. From the image, it is clear that the PM is the most susceptible region with a lot of severe localized corrosion sites. In the friction stir weldment of the AA2198-T851 alloy, the PM, with the highest volume fraction of the hexagonal T1 Al_2CuLi phase, is the most susceptible region to severe localized corrosion. The corrosion resistance reduces from the PM to the centre of the weld in accordance with the reduction in the volume fraction of the T1 phase from the PM to the SZ where the T1 phase is rarely found. These have been presented in recently published works of ours [4,6].

The optical and SEM micrographs presented in Fig. 2 show the morphology of the severe localized corrosion (SLC) observed on the PM. Some SLC sites were also observed on the HAZ adjacent to the TMAZ (Fig. 3a–b), but the extent of corrosion was not as pronounced as those observed in the PM/HAZ region further away from the TMAZ. The optical images presented in Fig. 3 reveal the corrosion morphology observed in the HAZ. Unlike the PM, the protected ringed regions surrounding the SLC pits were not pronounced because of the presence of corrosion products, and these regions were possibly re-passivated. Whereas, for the PM, the protected regions were very evident because the SLC was more pronounced and continuous, which resulted in the production of hydrogen ions and low pH in the vicinity of the pits. In aerated near-neutral NaCl solutions, the cathodic reaction outside the SLC sites is predominantly oxygen reduction reaction. Inside the pits, hydrolysis of water occurs through the reaction of H_20 and Al^{3+}. This produces H+ which results in hydrogen bubble evolution from the pits. The conditions inside the pits promote local acidification since oxygen is depleted inside the pits. The corrosion morphology of the SLC reveals that the attacks were mostly in bands. These bands have been attributed to the effect of the non-uniform distribution of the T1 phase [5,15]. However, analysis of the corrosion morphology is beyond the scope of this work, and more details have been presented elsewhere [15,16].

The SZ is resistant to severe localized corrosion and only exhibits a non-severe localized form of corrosion. However, localized corrosion products associated with the activities of cathodic intermetallic particles were observed in the SZ. These products were more pronounced in the advancing side of the weld (Fig. 3c) compared with the retreating side of the weld (Fig. 3d). The advancing side of friction stir weld usually contains more particles because the flow-arm of the weldment, which contains more particles than the other regions of the weld due to the action of the tool shoulder is located in this region [21,22]. Presented in Fig. 4 are SEM images showing the corroded surface of the SZ. The images were obtained after desmutting the sample in nitric acid for 5 min. These images show the corrosion products associated with the coarse particles found in the AS side of the SZ. However, the interesting features in these images are the minute cavities uniformly distributed across the surface. This sort of uniformly spread superficial attack is associated with the activities of Cu-rich particles which are either $T_B(Al_7Cu_4Li)$or T2 (Al_6CuLi_3) particles or a combination of both as explained below.

Examination of the uncorroded surface of the SZ revealed that it is composed of well-spread particles suspected to be T_B (Al_7Cu_4Li)/ T2 (Al_6CuLi_3) particles (Fig. 5). These particles are also preferentially precipitated at the grain boundaries in the TMAZ (see the inset in Fig. 5a) but are rarely found in the PM (Fig. 5c–d). The predominant micro-scale particles in the PM are the Cu-Fe rich particles [6] aligned as stringers in the rolling direction. The TEM analysis of the SZ (Fig. 6) further confirms that the uniformly spread particles in the SZ are predominantly Cu-rich particles, and are different from the coarse constituent Cu-Fe rich particles (Fig. 7). The presence of T_B particles in the weld zones of Al-Cu-Li alloys following

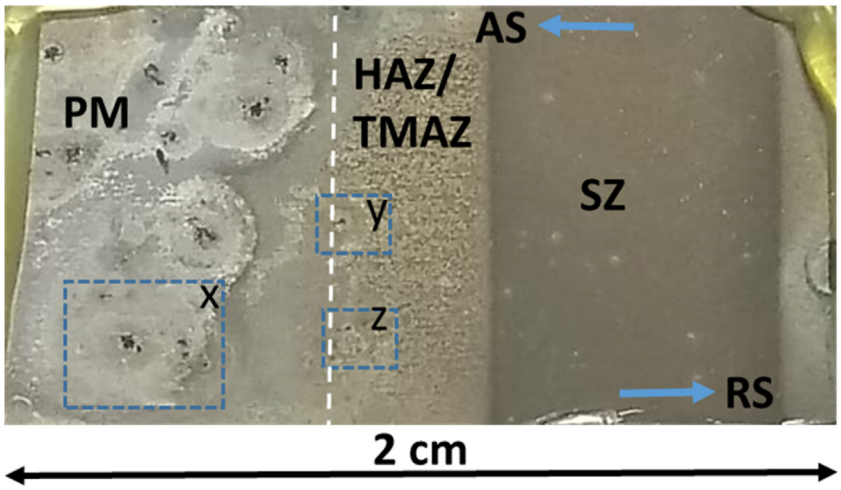

Fig. 1 – Optical macrograph of the AS of the friction stir weldment of the AA2198-T851 alloy after 72 h exposure to 5 mM NaCl solution.

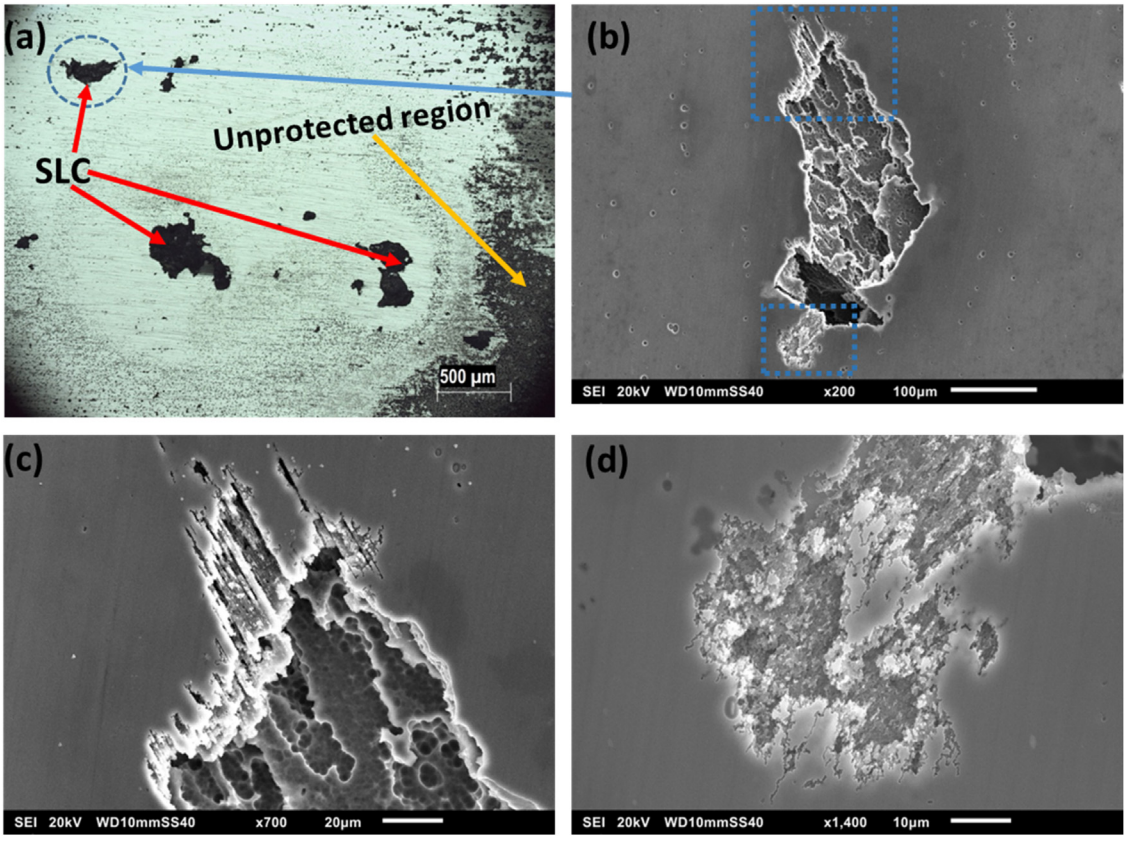

Fig. 2 – (a) Optical image of the fringed region X in Fig. 1, and (b)-(d) SEM images of the circled region in (a) showing the corrosion morphology of the SLC in the PM of the AA2198-T851 weldment.

the dissolution or partial dissolution of the T1 phase has been well reported [23–25]. An example can be found in the work of Fonda and Bingert where the presence of T_B particles in the SZ of a friction stir welded AA2195 Al-Cu-Li alloy was confirmed [24]. They revealed that the T_B particles nucleate from the spherical δ'/β' (Al_3 (Li, Zr)) precipitates. The presence of Zr at the base of some of the particles as indicated by the red arrows in Fig. 6 agrees with the revelation of Fonda and Bingert.

In fact, with the aid of diffraction patterns and high-resolution TEM imaging, Rao et al. confirmed the precipitation of T_B particles in the SZ of a friction stir welded 2198 Al alloy [25]. The high temperature reached in the SZ favours the dissolution of T1 particles and the precipitation of T_B/ T2 particles which are the predominant phases in overaged tempers of Al-Cu-Li alloys [26,27]. The T_B and T2 phases form more readily and coexist at temperatures above 300 °C [26–29] (such as the one

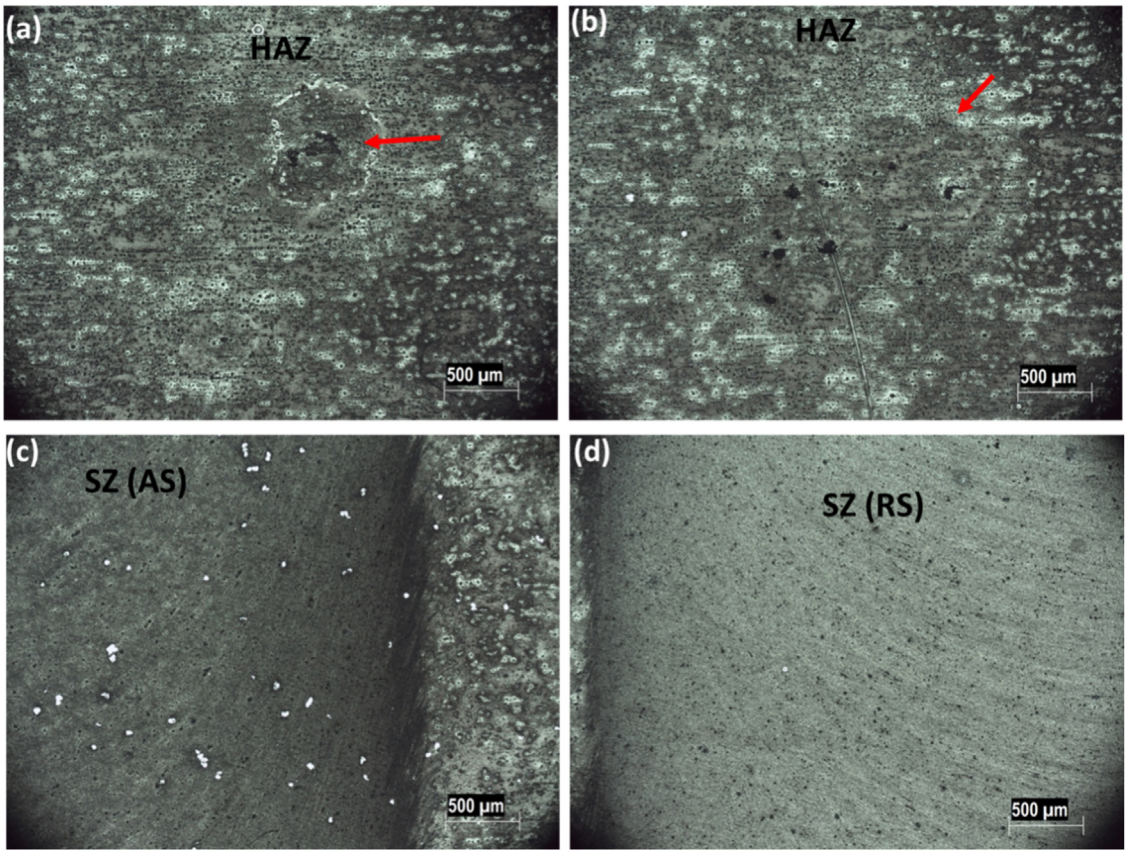

Fig. 3 – (a)-(b) Optical images of the HAZ (obtained from the fringed regions Y and Z in Fig. 1), and those of the SZ of the (c) AS and (d) RS after 72 h immersion test in 5 mM NaCl solution.

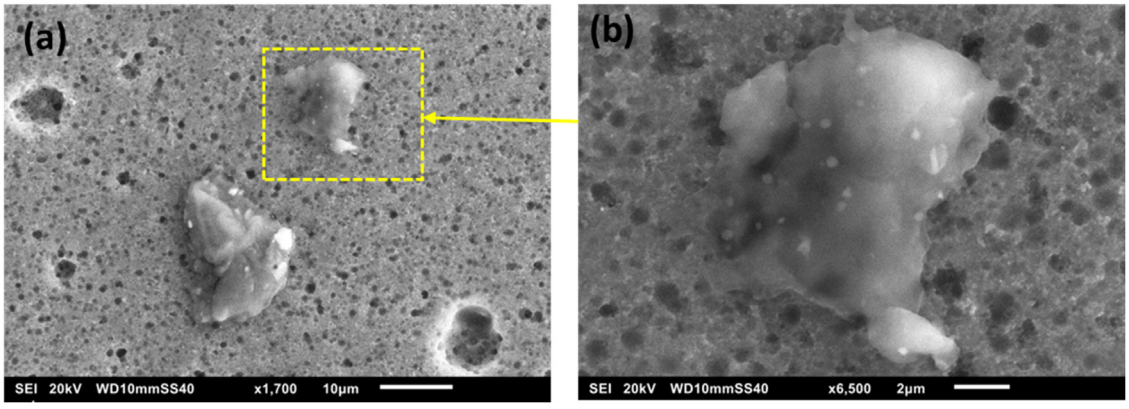

Fig. 4 – SEM images of the corroded surface of the SZ obtained in the AS region.

experienced in the SZ region during friction stir welding). This was evident in the work of Ovri [27], where the T_B, T2 and δ'/β' precipitates where the predominant phases in an Al-Li alloy aged at 370 °C. The metastable T1, θ and Ω phases were rapidly formed and dissolved at this temperature.

Furthermore, the DSC which is a very useful technique in the study of the phases precipitated in an Al alloy [30] and the different zones of its weldment [31] was also employed to further show the differences in the evolution of precipitates in the PM and SZ. Presented in Fig. 8 are DSC plots of the PM and the SZ showing exothermic and endothermic peaks associated with the precipitation and dissolution of different phases at different temperature ranges. On the SZ curve, the first endothermic process (A1) around 100 °C is associated with the dissolution of Guinier Preston (GP) zones [31]. The second endothermic process (B1) at about 210 °C corresponds to the dissolution of δ' particles. These two endothermic processes suggest that the GP zones and δ' particles were precipitated in this zone. Two exothermic peaks were observed within the temperature range of 210–360 °C. The first, labelled as C1′, corresponds to the precipitation of T1 particles, while the second, labelled C1″, corresponds to the thickening or coarsening

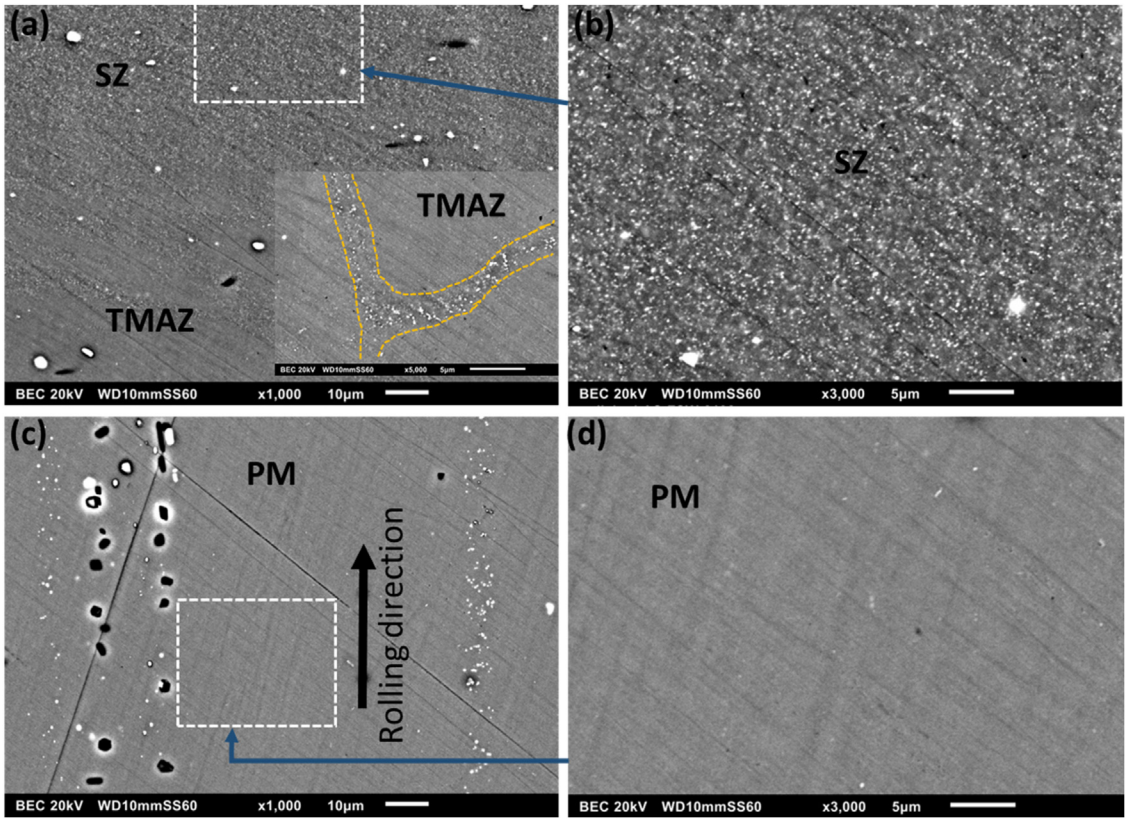

Fig. 5 – SEM images showing the distribution of suspected TB/T2 particles in the SZ, TMAZ and PM of the friction stir weldment of the AA2198-T851 alloy.

of the T1 particles [31–33]. Gumbmann et al. [32] and Dorin et al. [33] have shown that these peaks are solely attributed to the activities of the T1 phase because no streaks or evidence of other phases were recorded on small-angle x-ray scattering (SAXS) patterns within this temperature range. Based on this finding, it was proposed that the T1 precipitate forms via two mechanisms: rapid single layer growth followed by a slow thickening of the precipitate [33]. The high-temperature endothermic process (D1) around 400 °C is associated with the activities (dissolution) of the T_B/T2 particles. According to Gao et al. [30], the endothermic process of T2 particle occurs between 400–500 °C. Furthermore, another endothermic process (E1) was observed above 440 °C, and this is generally attributed to the general dissolution high-temperature particles. For the PM curve, endothermic activities corresponding to the dissolution of GP zones and δ' particles were not observed, and the exothermic peaks (C2′ and C2″) associated with the precipitation of T1 particles were not pronounced because T1 particles were already abundantly precipitated in this region. Also, the endothermic activity corresponding to the dissolution of the T_B/T2 particles was not observed or pronounced as that of the SZ, suggesting that these particles were not in abundance (if present at all) in the PM. Thus, from the DSC curves, it is evident that the T1 phase was dissolved in the SZ but was abundant in the PM, and the T_B/T2 particles were predominantly precipitated in the SZ. The T_B/T2 particles only result in superficial corrosion [6,34,35], and the uniform distribution of these particles in the SZ enhanced the rapid formation of a uniform protective film in this region. The T_B/T2 particles also cause superficial intergranular attacks in the TMAZ and HAZ closest to the SZ [6].

3.2. *Galvanic effects*

Presented in Fig. 9 are the potentiodynamic polarization curves of the PM and SZ regions. Both curves exhibit noticeable pseudo-passivity within small potential ranges immediately above the active regions as illustrated in the Figure. In this alloy, stable pitting sites are usually formed within 1 h of exposure to 5 mM NaCl solution. Thus, SLC sites were initiated during OCP measurements. The observed pseudo-passivation occurred as a result of the formation of a non-protective oxide layer [36,37]. This means that the surfaces were only partially passivated and active pitting sites were already initiated at potentials lower than the pseudo-passive potential ranges [36,37]. However, in these potential ranges, the contribution of the pitting current to the total current from the sample is overshadowed by the contribution from the pseudo-passive current [37]. This is because the pseudo-passive current is flowing from a larger surface area compared with the current flowing from the small pitting areas [37]. Above the pseudo-passive range, the contribution of the pits become significant, contributing more to the total current from the sample (compared with the pseudo-passive current) and resulting in high current density values per potential increase.

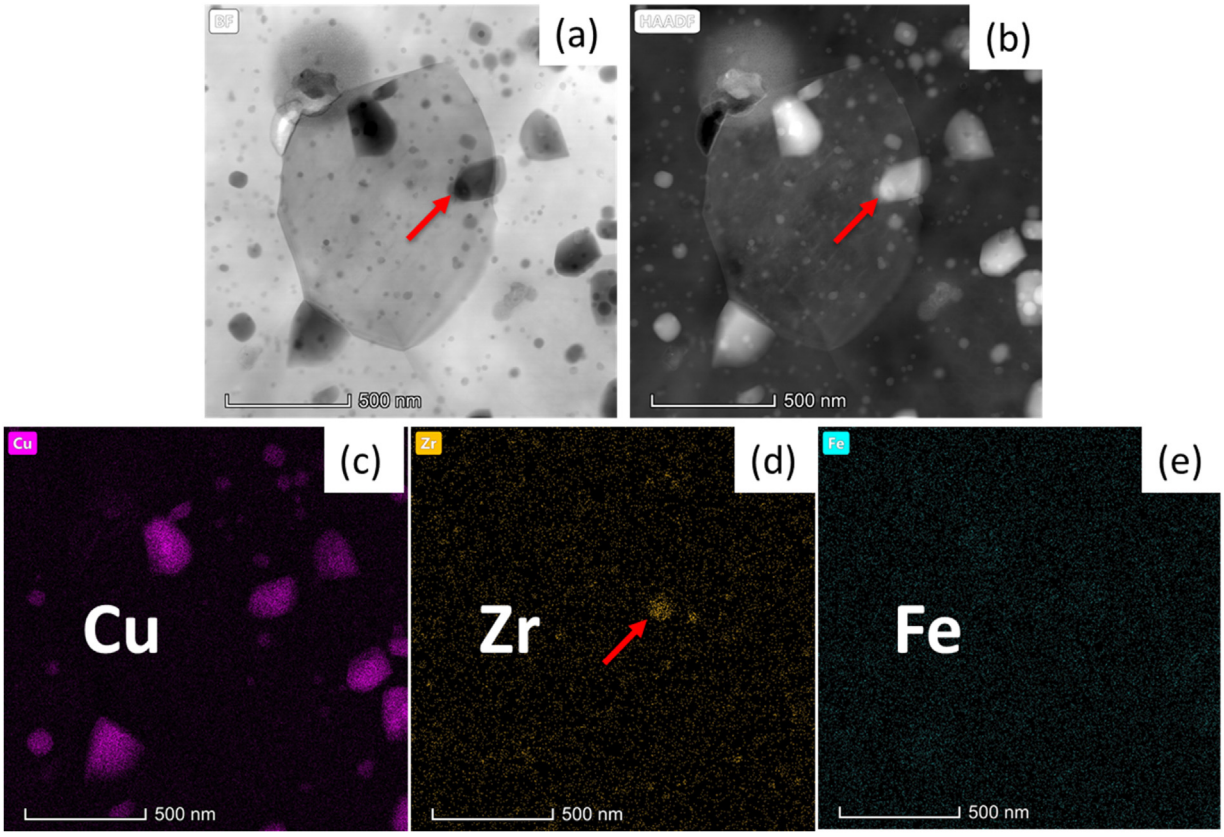

Fig. 6 – (a)-(b) Bright field and high angle annular dark field images of the SZ. (c)-(e) EDX maps of the imaged zone showing the distribution of Cu, Zr and Fe, respectively.

Nonetheless, it is evident that the PM (with the lower E_{corr} of −0.60 V) has more corrosion tendencies compared with the SZ (with an E_{corr} value in the range of -0.49 V). The difference in the E_{corr} values between the PM and SZ is about 100 mV, and this is far more than the 50 mV difference that has been termed the potential difference limit for the occurrence of galvanic corrosion. Thus, it is expected that a coupled system comprising the SZ and PM would result in galvanic interactions between the two regions with the PM being the anode. The galvanic potential (E_{galv}) of the system would be higher than the corrosion and pitting potentials of the PM. This means that the galvanic interactions would lead to more corrosion attack on the PM compared with when it is exposed in isolation. On the other hand, the SZ would also be more protected compared with when isolated. (Emphasis was not placed on the current density values from the polarization curves in a bid to quantify the extent of pitting attack on the SZ and PM, in isolation and when coupled. This is because it is difficult to establish the exact active areas involved in the pitting process as emphasized by Frankel [38]). Fig. 10 displays the optical images of the anodic PM (Fig. 10a) and the combination of the cathodic regions(the HAZ, TMAZ and SZ (Fig. 10b)) with respect to the PM. The PM in isolation exhibited less SLC sites per square area (14/cm^2) compared with the coupled PM(32/cm^2) in Fig. 1. The widths and depths of attacks for either case were not presented because they appeared to be in the same range for both cases, and were difficult to differentiate. Generally, the widths ranged from 60 to 420 μm and the depths of the attack were in the range of 37–41 μm in both cases. Thus, the attack propagated more laterally than through the thickness of the alloy.

Interestingly, the isolated cathodic region shows that the SZ (Fig. 10b), which did not exhibit any form of SLC when coupled with the PM, presented SLC when exposed in isolation (Fig. 11). This is also evident from the images showing the ring-like protected area around each SLC site (just like what was observed on the PM). These protected regions are cathodic to the SLC sites and should act as efficient cathodes. More details are revealed in the SECM section below. Furthermore, SLC sites were mainly observed in the AS of the weld. A careful examination of the corrosion morphology shows that the attacks preferentially occurred in bands according to the tool shoulder motion. SEM micrographs of the unexposed surface of the SZ (Fig. 12) show alternate bands of particle-rich domains in the AS. These features were not found on the RS of the SZ. Two types of particle bands can be observed: the dark and bright bands. The dark bands are most likely from Li-rich particles while the bright bands are from Cu and Cu-Fe rich particles as detected by EDX. (The presence of Li was difficult to establish since Li cannot be detected using the EDX detector equipped in the JEOL JSM-6010 LA microscope). Thus, micro-galvanic coupling occurs between the particle-rich domain and the adjacent matrix within the AS of the SZ, and this results in the formation of SLC in the bands. Based

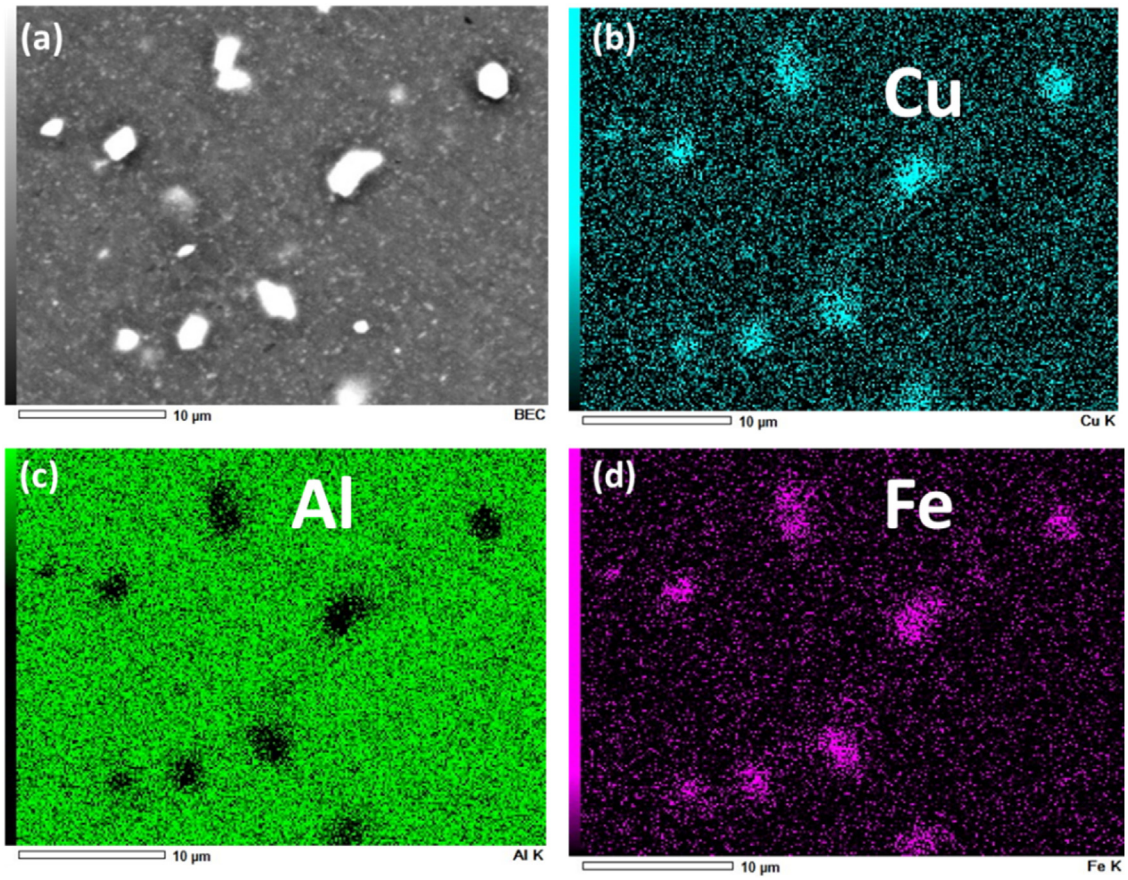

Fig. 7 – SEM-EDX maps of fragmented Cu-Fe rich particles in the SZ.

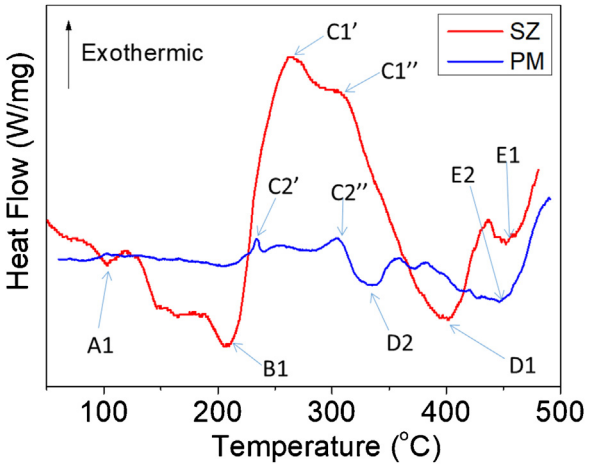

Fig. 8 – DSC thermograms obtained using samples from the SZ and PM of the AA2198-T851 weldment.

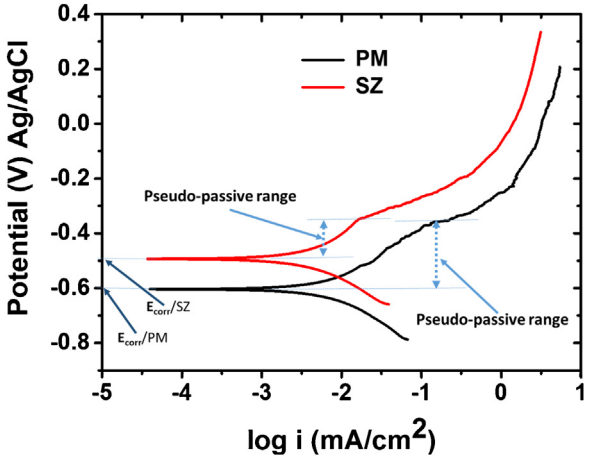

Fig. 9 – Potentiodynamic polarization curves of the PM and SZ of the friction stir weldment of the AA2198-T851 alloy. The curves were obtained in 5 mM NaCl solution.

on the fact that Cu-Fe rich particles mainly cause the formation of trenches and micro-pits, it is suggested, herein, that the Li-rich bands were the preferential SLC sites on the SZ.

3.3. *Scanning electrochemical microscopy (SECM)*

The SECM results presented in this work were obtained in competitive and substrate generation/tip collection (SG/TC) modes. SECM tests were carried out in this study in two modes. First, in the competitive mode, to evaluate the molecular oxygen content from its electro-reduction at the tip polarized at −0.7 V (Ag/AgCl). This allows a comparative evaluation of the current associated with oxygen reduction. Larger currents mean that less oxygen is consumed by the corrosion activities at the surface. This technique was used only to

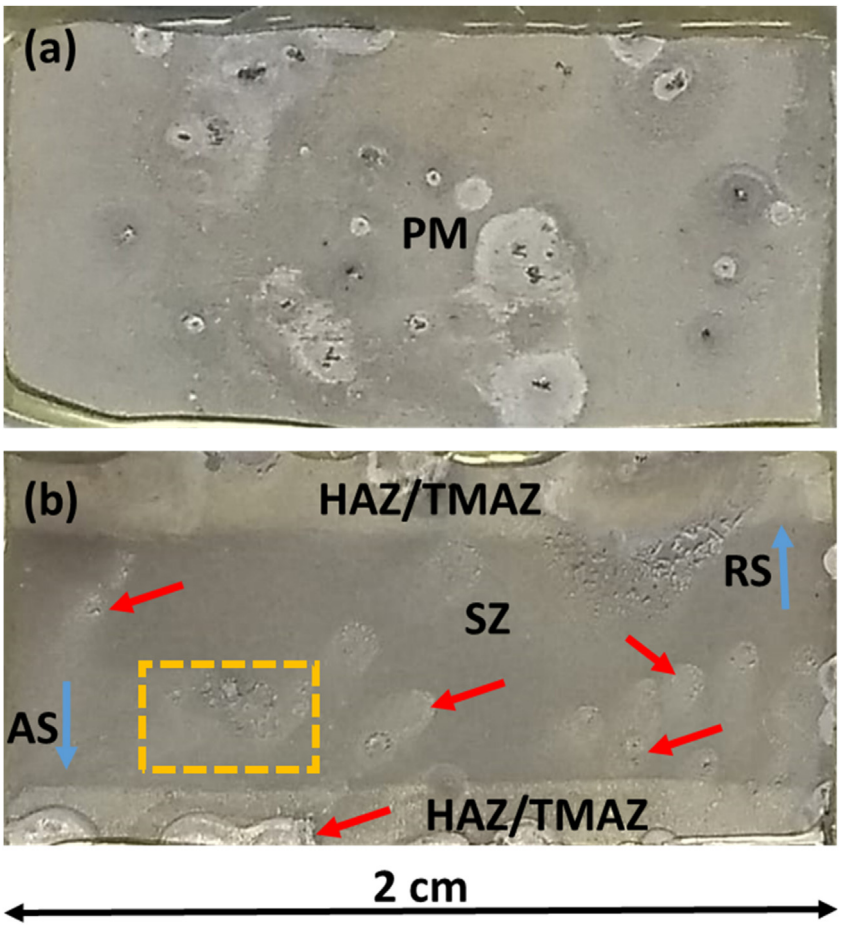

Fig. 10 – Optical macrograph of the (a) PM and (b) SZ – HAZ/TMAZ region after 72 h immersion test in 5 mM NaCl solution.

evaluate the oxygen activity at the surface and not the mechanism. Nonetheless, it is important to state that in near-neutral NaCl solutions, the cathodic reaction outside the SLC sites is predominantly oxygen reduction reaction. Inside the pits, hydrolysis of water occurs through the reaction of H_20 and Al^{3+}. This produces H^+ which results in hydrogen bubble evolution from the pits. The conditions inside the pits promote local acidification since oxygen is depleted inside the pits.

In the competitive mode, the molecular oxygen content was monitored from its electro-reduction at the tip at −0.70 V (Ag/AgCl) (reaction 3) in aerated 5 mM NaCl solution.

$$O_2 + 2H_2O + 4e^- \rightarrow 4OH^- \quad (3)$$

The SECM measurements were obtained from the mid-part of the SZ to the PM side of the AS of the weldment. Fig. 13 presents the current maps associated with oxygen reduction after 1 h of exposure to 5 mM NaCl solution. The maps show a clear current distribution contrast associated with the amount of dissolved oxygen consumption between the PM and the other zones. Presented in Fig. 14 are the line scans for oxygen reduction current (Fig. 14a) and current related to hydrogen generation (Fig. 14b). H_2 generation can be sensed at a potential of 0.0 V (Ag/AgCl) in an oxidation reaction (reaction 4) at the UME tip under the SG/TC mode.

$$H2 \rightarrow 2H^+ + 2e^- \quad (4)$$

Equation (4) corresponds to the anodic reaction of molecular hydrogen oxidation. This occurs at the tip polarized at 0.0 V (Ag/AgCl) and it was used to evaluate hydrogen production at the surface, mainly at the severe localized corrosion (SLC) sites. Thus, this technique also evaluates the activity at the surface of the exposed alloy by oxidizing the products of the active sites at the tip but not the corrosion mechanism.

Figs. 13 and 14 show that the current associated with oxygen reduction was higher on the HAZ/TMAZ (region b (as high as 200 nA)) and SZ (region c (range of 140 nA)) compared with the PM (region a (20–30 nA)). This indicates that less oxygen was being consumed by the corrosion activities occurring on the surface, at the HAZ/TMAZ and SZ regions. It is also very evident from the line scan of oxygen reduction current that the HAZ/TMAZ region exhibited the highest current associated with oxygen reduction. Away from the boundary, the values of the oxygen reduction current dropped significantly, but not to levels as low as those recorded on the PM. The variation observed, in the levels of depleted dissolved oxygen, is surprising because higher oxygen depletion was expected on the

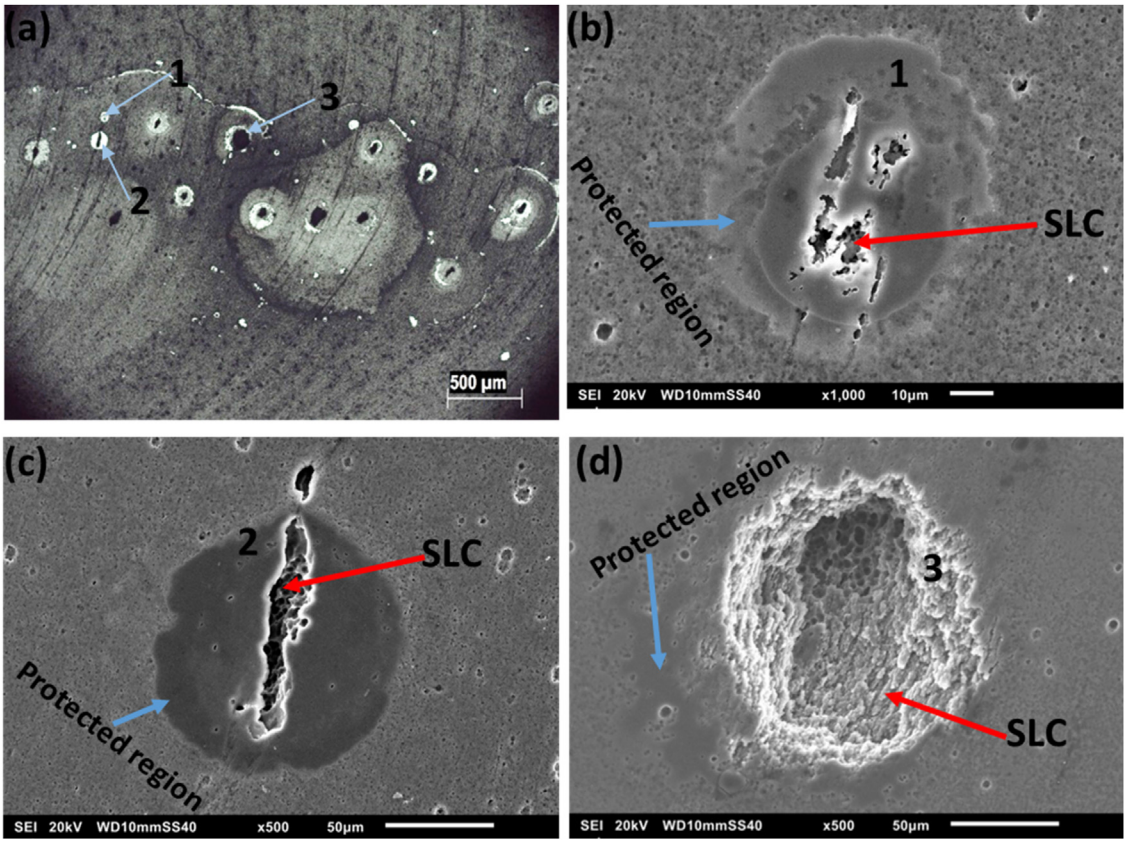

Fig. 11 – (a) Optical image of the fringed region in Figure 10b and (b)-(c) SEM images of the regions labelled 1, 2 and 3 in.(a).

HAZ/TMAZ and SZ since these regions were cathodic to the PM. What was expected is the depletion of dissolved oxygen near the cathode because the tip is biased in the potential range at which oxygen reduction proceeds [39]. In the SECM mode employed, a decrease in reduction current indicates the depletion of the species (dissolved oxygen in this case) since the biased tip and surface of the substrate compete for the species [40]. However, the level of dissolved oxygen depletion was higher in the PM (which is the most anodic region) indicating that more amount of dissolved oxygen was being consumed in this region. As earlier shown in Figs. 1 and 2, each SLC site in the PM region is surrounded by a ring-like protected region (far more protected compared with the HAZ/TMAZ and the SZ). Given the proximity to the SLC anodic site, it is logical to assume that the protected region would act as a more efficient cathode for the promotion of the severe pitting process in the SLC site. To establish the predominant cathodic reaction occurring in the protected region, SECM current measurements associated with H_2 evolution and oxygen consumption around selected pits on a corroded PM substrate (that was tested in isolation) were recorded. The SECM results (Fig. 15a) indicate that oxygen consumption was more predominant in the region just outside the protected region. Oxygen consumption was lowest on the pit, as expected, and was higher in the protected region (compared with the pit) but was highest at regions bordering the protected region. In contrast, H_2 evolution (Fig. 15b) was most pronounced on the pit but was also pronounced on the protected region around the pit compared with the regions outside the protected area. This implies that, although the predominant reduction of H^+ to generate H_2 bubbles occurs inside the pits, hydrogen ions are also reduced around the pit mouth since H^+ ions migrate from within the pit to the pit mouth due to electrostatic potential difference [41]. Thus, the protected regions around the pit mouths were efficient cathodes based on H_2 evolution reactions and not based on oxygen reduction reactions, since the regions for the reduction of oxygen on the anodic PM were the regions outside the protected regions surrounding the pits.

For the HAZ/TMAZ region, the level of oxygen consumption is lower compared with the PM possibly because the SLC sites were few, and not active enough to promote strong oxygen reduction reactions in the cathodic regions immediately surrounding the pits (compare the image in Fig. 2a to those in 3 a-b). Thus, the cathodic efficiency of the HAZ/TMAZ region was very low. On the other hand, the SZ consumes more oxygen than the HAZ/TMAZ region because it is more cathodic. However, it does not consume dissolved oxygen as much as the regions outside the protected areas around the pits in the PM. This is most likely because of the activities of the uniformly distributed T_B/ T2 particles. These particles cause superficial general corrosion, as evident in Fig. 4 above, but result in the formation of a uniformly formed corrosion product on the surface in this region. The uniformly distributed corrosion product on the SZ renders the surface less cathodic efficient (compared with the regions immediately outside the protected region in the vicinity of the severe localized cor-

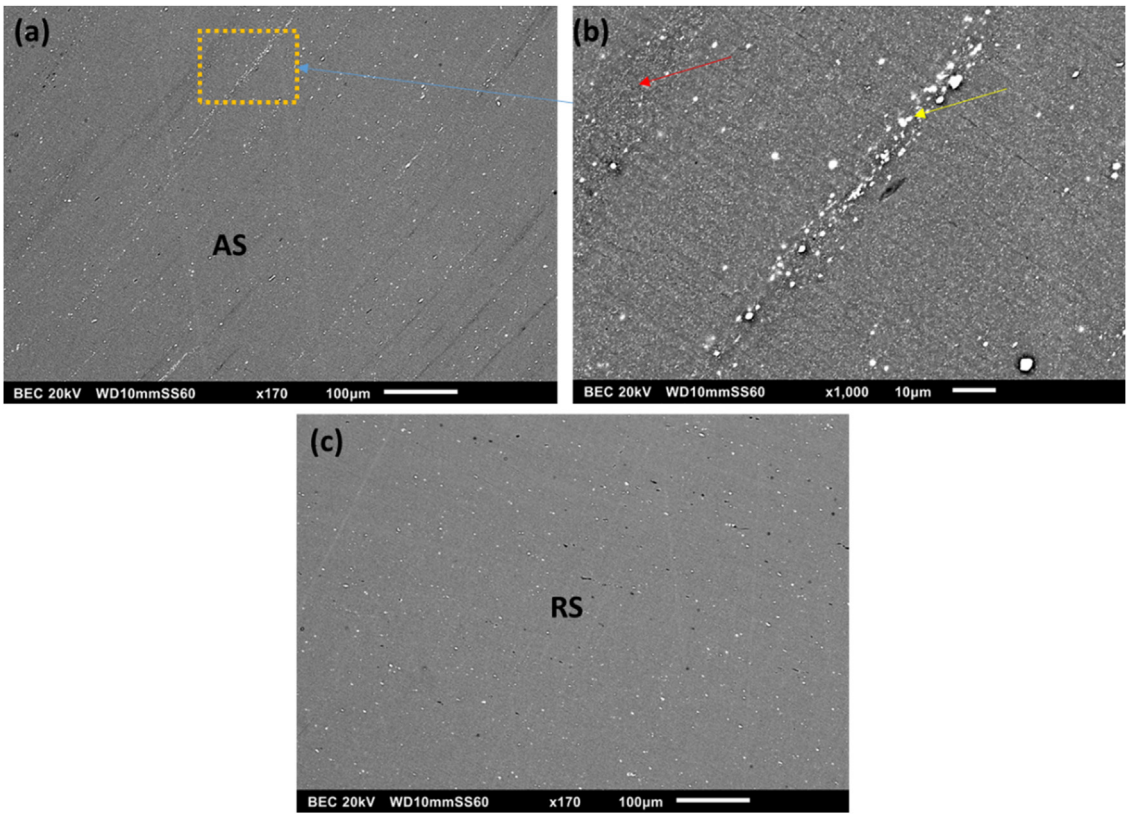

Fig. 12 – SEM images of the (a)-(b) AS and (c) RS of the polished surface of the SZ of the AA2198-T851 weldment.

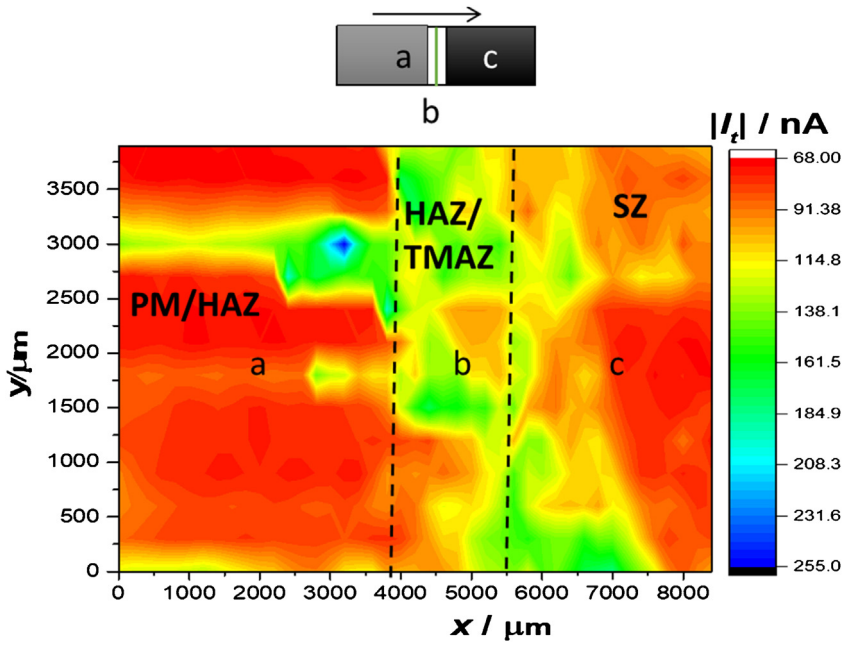

Fig. 13 – SECM map of the oxygen reduction current across the AS of the friction stir weldment of the AA2198-T851 alloy.

rosion (SLC) sites on the PM) in terms of oxygen reduction because it is more resistant.

The areas surrounding the protected regions consume dissolved oxygen better than the bulk cathodic regions (HAZ/TMAZ and SZ) owing to its proximity to the SLC site. Two factors make the SZ less cathodic efficient compared with the protected regions and the regions bordering the protected regions around the SLC sites: the distance from the SLC

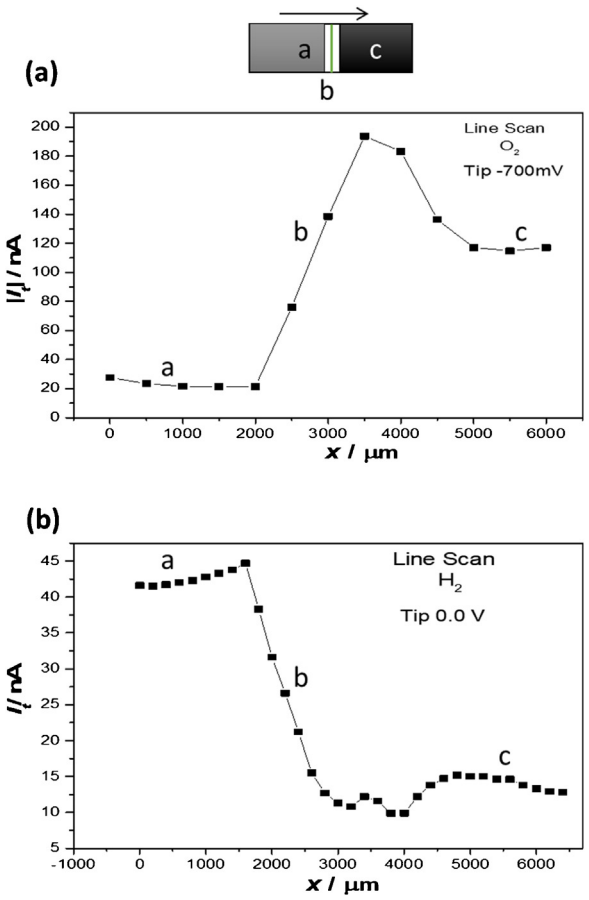

Fig. 14 – SECM line scans of the current values associated with(a) oxygen reduction and (b) hydrogen generation across the AS of the friction stir weldment of the AA2198-T851 alloy.

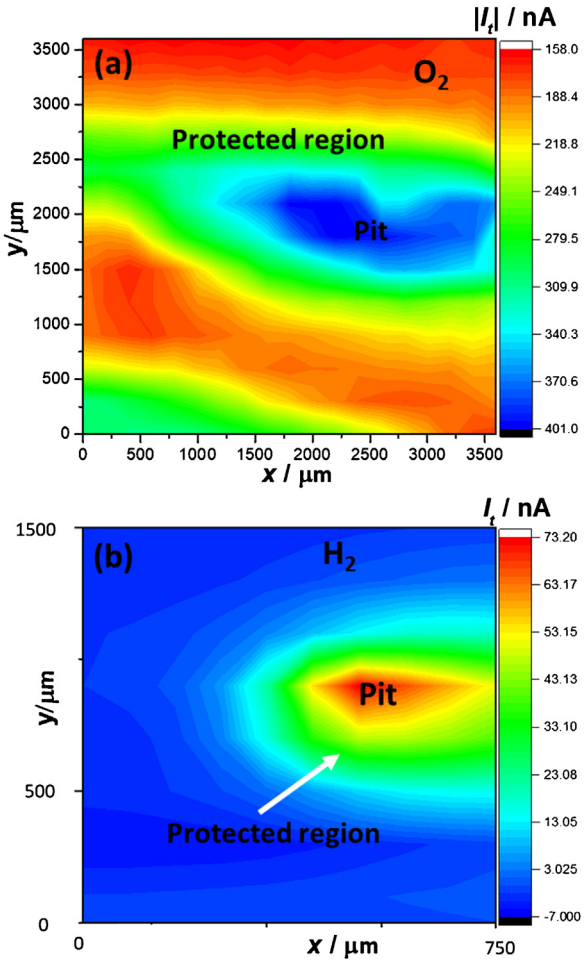

Fig. 15 – SECM current maps associated with (a) oxygen reduction and (b) hydrogen evolution around pits on an isolated PM region.

sites and the uniformly formed corrosion products. However, it must be stated that galvanic interactions between the zones exist, and this is evident from the lack of SLC sites on the SZ when it is coupled, which are appreciably formed when the zone is isolated.

The reduction of oxygen in the vicinity of the anodic region as discussed above is similar to what was observed by Snihirova et al. [42] and confirmed by Silva et al. [43] As reported by Snihirova et al. [42], oxygen depletion was observed in the vicinity of an active Mg substrate which was coupled to Cu and Al substrates. However, the highest level of depletion was observed on the Cu substrate as expected, but the level of oxygen depletion on the Mg substrate was far lower than that observed in the Al substrate. The purging effect of H_2 evolution on the depletion of dissolved oxygen was later studied [43], and it was observed that although the purging effect caused oxygen depletion to as low as 4 ppm, this value was far higher than the concentration levels of less than 1 ppm observed during corrosion. It was empirically shown that oxygen reduction events did actually occur in the vicinity of the anodic region, and this is in agreement with the results presented in this study.

Furthermore, the hydrogen generation line scan shows that more hydrogen bubbles were being evolved on the PM (42–45 nA) compared with the HAZ/TMAZ (8–13 nA) and the SZ (13–15 nA). As earlier revealed, the PM is the most susceptible region to SLC due to the significant presence of the T1 phase. Given that hydrogen evolution is a primary feature of the SLC as it results from the hydrolysis of Al ions from within the pits, it is not surprising to observe higher current values associated with hydrogen generation on the PM compared with the other zones; since the other zones exhibit fewer SLC (HAZ) or no SLC sites. Also, it is important to note that the current values associated with hydrogen generation were lowest at the galvanic boundary (between the HAZ/TMAZ). This suggests that the dissolution activities at this boundary were the least on the average and this zone was also the least cathodic efficient both in terms of hydrogen evolution and oxygen reduction. Away from the HAZ/TMAZ region, the hydrogen evolution activities increased slightly on the SZ because of the activities of the T_B/ T2 particles. However, the formation of uniformly formed corrosion products from the activities of these particles prevents the development of SLC sites, in addition to the galvanic protection rendered by the pronounced SLC activities on the PM. Thus, in a galvanic couple of the weldment, the cathodic HAZ/TMAZ region closest to the anodic PM consumes the least

amount of dissolved oxygen because of the absence of efficient cathodic sites and is the least active in terms of anodic activities resulting in low hydrogen evolution compared with the SZ and PM regions.

4. Conclusions

The macro and micro-galvanic corrosion within and between the zones in friction stir weldment of the AA2198-T851 alloys have been investigated, and the following conclusions can be drawn.

The PM is the most anodic region in the weldment and the region that is most susceptible to SLC due to the high population density of T1 particles in this region. The SZ, with no trace of T1 particles, does not exhibit SLC when coupled with the PM and HAZ. However, the SZ exhibits SLC in the AS when tested in isolation. The SLC in the AS of the SZ results from the micro-galvanic interactions between banded regions richer in particles and their surroundings.

The SECM proved to be a powerful tool in establishing extents of galvanic interactions. The SECM results revealed higher currents associated with oxygen reduction in the HAZ/TMAZ and SZ compared with the PM because the regions surrounding the SLC sites on the PM act as more efficient cathodes compared with the bulk cathodic regions comprising the SZ, HAZ and TMAZ. Furthermore, hydrogen generation current values were higher in the PM (compared with the other zones), which agrees with the higher SLC observed in this region since hydrogen evolution is a prominent feature of SLC due to hydrolysis.

Conflicts of interest

The authors declare no conflicts of interest.

Acknowledgement

The authors thank São Paulo Research Foundation (FAPESP), Brazil for financial support through the grant Proc. 2013/13235-6 and for sponsoring the postdoctoral fellowship of Dr Uyime Donatus (Process 2017/03095-3) and Dr Rejane Maria Pereira da Silva (Process 2018/06880-6).

REFERENCES

[1] Dursun T, Soutis C. Recent developments in advanced aircraft aluminium alloys. Mater Des 2014;56:862–71, http://dx.doi.org/10.1016/j.matdes.2013.12.002.
[2] Rioja RJ, Liu J. The evolution of Al-Li base products for aerospace and space applications. Metall Mater Trans A Phys Metall Mater Sci 2012;43:3325–37, http://dx.doi.org/10.1007/s11661-012-1155-z.
[3] Zhang X, Liu B, Zhou X, Wang J, Luo C, Sun Z, et al. Corrosion behavior of friction stir welded 2A97 Al-Cu-Li alloy. Corrosion 2017;9312:2418, http://dx.doi.org/10.5006/2418.
[4] Donatus U, Ferreira RO, Mogili NVV, Viveiros BVGde, Milagre MX, Costa I. Corrosion and anodizing behaviour of friction stir weldment of AA2198-T851 Al-Cu-Li alloy. Mater Chem Phys 2018;219:493–511, http://dx.doi.org/10.1016/j.matchemphys.2018.08.053.
[5] Zhang X, Zhou X, Hashimoto T, Liu B, Luo C, Sun Z, et al. Corrosion behaviour of 2A97-T6 Al-Cu-Li alloy: the influence of non-uniform precipitation. Corros Sci 2018;132:1–8, http://dx.doi.org/10.1016/j.corsci.2017.12.010.
[6] Donatus U, de Viveiros BVG, de Alencar MC, Ferreira RO, Milagre MX, Costa I, et al. Correlation between corrosion resistance, anodic hydrogen evolution and microhardness in friction stir weldment of AA2198 alloy. Mater Charact 2018;144:99–112, http://dx.doi.org/10.1016/j.matchar.2018.07.004.
[7] Buchheit RG, Moran JP, Stoner GE. Localized corrosion behavior of alloy 2090—the role of microstructural heterogeneity. Corrosion 1990;46:610–7, http://dx.doi.org/10.5006/1.3585156.
[8] Buchheit RG, Moran JP, Stoner GE. Electrochemical behavior of the T1 (Al2CuLi) intermetallic compound and its role in localized corrosion of Al-2%Li-3%Cu alloys. Corrosion 1994;50:120–30, http://dx.doi.org/10.5006/1.3293500.
[9] Li JF, Li CX, Peng ZW, Chen WJ, Zheng ZQ. Corrosion mechanism associated with T1 and T2 precipitates of Al-Cu-Li alloys in NaCl solution. J Alloys Compd 2008;460:688–93, http://dx.doi.org/10.1016/j.jallcom.2007.06.072.
[10] lei Huang J, feng Li J, yang Liu D, feng Zhang R, lai Chen Y, hu Zhang X, et al. Correlation of intergranular corrosion behaviour with microstructure in Al-Cu-Li alloy. Corros Sci 2018;139:215–26, http://dx.doi.org/10.1016/j.corsci.2018.05.011.
[11] Yan Y, Peguet L, Gharbi O, Deschamps A, Hutchinson CR, Kairy SK, et al. On the corrosion, electrochemistry and microstructure of Al-Cu-Li alloy AA2050 as a function of ageing. Materialia 2018;000:1–12, http://dx.doi.org/10.1016/j.mtla.2018.05.003.
[12] Ralston KD, Birbilis N, Cavanaugh MK, Weyland M, Muddle BC, Marceau RKW. Role of nanostructure in pitting of Al-Cu-Mg alloys. Electrochim Acta 2010;55:7834–42, http://dx.doi.org/10.1016/j.electacta.2010.02.001.
[13] Kairy SK, Rometsch PA, Diao K, Nie JF, Davies CHJ, Birbilis N. Exploring the electrochemistry of 6xxx series aluminium alloys as a function of Si to Mg ratio, Cu content, ageing conditions and microstructure. Electrochim Acta 2016;190:92–103, http://dx.doi.org/10.1016/j.electacta.2015.12.098.
[14] Gupta RK, Deschamps A, Cavanaugh MK, Lynch SP, Birbilis N. Relating the early evolution of microstructure with the electrochemical response and mechanical performance of a Cu-Rich and Cu-Lean 7xxx aluminum alloy. J Electrochem Soc 2012;159:C492–502, http://dx.doi.org/10.1149/2.062211jes.
[15] Donatus U, Terada M, Ospina CR, Queiroz FM, Fatima Santos Bugarin A, Costa I. On the AA2198-T851 alloy microstructure and its correlation with localized corrosion behaviour. Corros Sci 2018;131:300–9, http://dx.doi.org/10.1016/j.corsci.2017.12.001.
[16] de Sousa Araujo JV, Donatus U, Queiroz FM, Terada M, Milagre MX, de Alencar MC, et al. On the severe localized corrosion susceptibility of the AA2198-T851 alloy. Corros Sci 2018;133:132–40, http://dx.doi.org/10.1016/j.corsci.2018.01.028.
[17] Proton V, Alexis J, Andrieu E, Blanc C, Delfosse J, Lacroix L, et al. Influence of post-welding heat treatment on the corrosion behavior of a 2050-T3 aluminum-copper-Lithium alloy friction stir welding joint. J Electrochem Soc 2011;158:C139, http://dx.doi.org/10.1149/1.3562206.
[18] Proton V, Alexis J, Andrieu E, Delfosse JÔ, Deschamps A, De Geuser F, et al. The influence of artificial ageing on the corrosion behaviour of a 2050 aluminium-copper-lithium

alloy. Corros Sci 2014;80:494–502, http://dx.doi.org/10.1016/j.corsci.2013.11.060.
[19] Proton V, Alexis J, Andrieu E, Delfosse J, Lafont M-C, Blanc C. Characterisation and understanding of the corrosion behaviour of the nugget in a 2050 aluminium alloy Friction stir Welding joint. Corros Sci 2013;73:130–42, http://dx.doi.org/10.1016/j.corsci.2013.04.001.
[20] Souto RM, Lamaka SV, González S. Uses of Scanning Electrochemical Microscopy in Corrosion Research. Microsc Sci Technol Appl Educ 2010;3:1769–80.
[21] Donatus U, Thompson GE, Zhou X, Wang J, Beamish K. Flow patterns in friction stir welds of AA5083 and AA6082 alloys. Mater Des 2015;83:203–13, http://dx.doi.org/10.1016/j.matdes.2015.06.006.
[22] Widener CA. Evaluation of post-weld heat treatments for corrosion protection in 2024 and 7075 aluminum alloys. Wichita State University; 2000.
[23] Chen DL, Chaturvedi MC. Effects of welding and weld heat-affected zone simulation on the microstructure and mechanical behavior of a 2195 aluminum-lithium alloy. Metall Mater Trans A Phys Metall Mater Sci 2001;32:2729–41, http://dx.doi.org/10.1007/s11661-001-1025-6.
[24] Fonda RW, Bingert JF. Precipitation and grain refinement in a 2195 Al friction stir weld. Metall Mater Trans A Phys Metall Mater Sci 2006;37:3593–604, http://dx.doi.org/10.1007/s11661-006-1054-2.
[25] Rao JC, Payton EJ, Somsen C, Neuking K, Eggeler G, Kostka A, et al. Where does the Lithium Go? - a study of the precipitates in the stir zone of a friction stir weld in a Li-containing 2xxx series Al alloy. Adv Eng Mater 2010;12:298–303, http://dx.doi.org/10.1002/adem.200900284.
[26] Lee YS. Microstructures in over-aged Al-Cu-Li-Mg-Ag alloys. J Mater Sci Lett 1998;17:1161–4, http://dx.doi.org/10.1023/A:1006500601447.
[27] Ovri H. Micromechanisms governing plastic instability in Al–Li based alloys. Helmholtz-Zentrum Geesthacht; 2015.
[28] Abozid EF, Gaber A, Gaffar MA, Galal L. Precipitation of Nano-sized Secondary Phases For Enhanced Alloy Hardeneing in an AL-LI-Alloy (2090). Int J Metall Mater Sci Eng 2013;3:69–82.
[29] CHEN PS, Bhat BN. Time-temperature-Precipitation behavior in AI-Li alloy 2195. Tech Rep 2002.
[30] Gao N, Starink MJ, Davin L, Cerezo A, Wang SC, Gregson PJ. Microstructure and precipitation in Al–Li–Cu–Mg–(Mn, Zr) alloys. Mater Sci Technol 2005;21:1010–8, http://dx.doi.org/10.1179/174328405X27034.
[31] Sidhar H, Mishra RS. Aging kinetics of friction stir welded Al-Cu-Li-Mg-Ag and Al-Cu-Li-Mg alloys. Mater Des 2016;110:60–71, http://dx.doi.org/10.1016/j.matdes.2016.07.126.
[32] Gumbmann E, De Geuser F, Sigli C, Deschamps A. Influence of Mg, Ag and Zn minor solute additions on the precipitation kinetics and strengthening of an Al-Cu-Li alloy. Acta Mater 2017;133:172–85, http://dx.doi.org/10.1016/j.actamat.2017.05.029.
[33] Dorin T, Deschamps A, De Geuser F, Lefebvre W, Sigli C. Quantitative description of the T_1 formation kinetics in an Al–Cu–Li alloy using differential scanning calorimetry, small-angle X-ray scattering and transmission electron microscopy. Philos Mag (Abingdon) 2014;94:1012–30, http://dx.doi.org/10.1080/14786435.2013.878047.
[34] Zhang X, Zhou X, Hashimoto T, Lindsay J, Ciuca O, Luo C, et al. The influence of grain structure on the corrosion behaviour of 2A97-T3 Al-Cu-Li alloy. Corros Sci 2017;116:14–21, http://dx.doi.org/10.1016/j.corsci.2016.12.005.
[35] Zhang X, Liu B, Zhou X, Wang J, Hashimoto T, Luo C, et al. Laser welding introduced segregation and its influence on the corrosion behaviour of Al-Cu-Li alloy. Corros Sci 2018;135:177–91, http://dx.doi.org/10.1016/j.corsci.2018.02.044.
[36] Viramontes-Gamboa G, Rivera-Vasquez BF, Dixon DG. The active-passive behavior of chalcopyrite. J Electrochem Soc 2007;154:C299–311, http://dx.doi.org/10.1149/1.2721782.
[37] Burstein GT, Salter VCC, Ball J, Sharman JD. In: Datta M, MacDougall BR, Fenton JM, editors. The growth of pits during the electrograining of aluminium. Chicago, Illinois, USA: Electrochemical Society; 1996.
[38] Frankel G. The effects of microstructure and composition on Al alloy corrosion. Corrosion 2015;71:1308–20.
[39] Simões A, Battocchi D, Tallman D, Bierwagen G. Assessment of the corrosion protection of aluminium substrates by a Mg-rich primer: EIS, SVET and SECM study. Prog Org Coatings 2008;63:260–6, http://dx.doi.org/10.1016/j.porgcoat.2008.02.007.
[40] Marques AG, Izquierdo J, Souto RM, Simões AM. SECM imaging of the cut edge corrosion of galvanized steel as a function of pH. Electrochim Acta 2015;153:238–45, http://dx.doi.org/10.1016/j.electacta.2014.11.192.
[41] Tsuyuki C, Yamanaka A, Ogimoto Y. Phase-field modeling for pH-dependent general and pitting corrosion of iron. Sci Rep 2018;8:12777, http://dx.doi.org/10.1038/s41598-018-31145-7.
[42] Snihirova D, Taryba M, Lamaka SV, Montemor MF. Corrosion inhibition synergies on a model Al-Cu-Mg sample studied by localized scanning electrochemical techniques. Corros Sci 2016;112:408–17, http://dx.doi.org/10.1016/j.corsci.2016.08.008.
[43] Silva EL, Lamaka SV, Mei D, Zheludkevich ML. The reduction of dissolved oxygen during magnesium corrosion. ChemistryOpen 2018;7:664–8, http://dx.doi.org/10.1002/open.201800076.